Incommensurate magnetic ordering and a possible structural transition in $EuIn_4$

D. H. Ryan*
Physics Department and Centre for the Physics of Materials, McGill University, 3600 University Street, Montreal, QC, H3A 2T8, Canada

Sergey L. Bud'ko and Paul C. Canfield
Ames National Laboratory, U.S. Department of Energy, Iowa State University, Ames, Iowa 50011-3020, USA
and Department of Physics and Astronomy, Iowa State University, Ames, Iowa 50011, USA

(Received 11 June 2024; accepted 6 September 2024; published 20 September 2024)

Single crystals of $EuIn_4$ were grown and ^{151}Eu Mössbauer spectroscopy, combined with temperature-dependent electrical resistance, specific heat, and anisotropic magnetization measurements have been used to investigate the magnetic ordering of monoclinic $EuIn_4$. We find two closely spaced magnetic transitions (at ∼10 K and ∼11 K). The initial ordering leads to an incommensurate sinusoidally modulated structure that squares up rapidly on cooling through the lower (10 K) transition. Well above the magnetic transitions, we observe an additional transition at ∼130 K which may also involve two closely spaced events. This upper transition(s) is most likely structural and offers no suggestion of magnetic nature either in magnetization or Mössbauer data.

DOI: 10.1103/PhysRevMaterials.8.094409

I. INTRODUCTION

Europium forms a series of $(Eu^{2+})X_4$ compounds with the group 13 metals (X=Al,Ga,In; $EuTl_4$ does not appear to exist, as only EuTl [1,2], $EuTl_2$ [3] and $EuTl_3$ [4,5] have been reported). Of these, $EuAl_4$ and $EuGa_4$ have been studied extensively, while only a structural study [6] appears to have been reported for $EuIn_4$. Whereas both $EuAl_4$ and $EuGa_4$ adopt the same tetragonal $BaAl_4$-type structure ($I4/mmm$ #139) with the europium atoms on the $2a$ site forming a *bct* lattice [7], $EuIn_4$ adopts a more complex monoclinic structure ($C2/m$ #12) [6]. Despite sharing a rather simple tetragonal structure, $EuAl_4$ and $EuGa_4$ exhibit very different magnetic properties. $EuGa_4$ exhibits simple basal-plane antiferromagnetic (AFM) ordering below $T_N = 16.5$ K [8], with the body center moments antiparallel to the corner ones [9]. By contrast, $EuAl_4$ undergoes a complex sequence of four magnetic transitions below 16 K [10]. Time-of-flight Laue neutron diffraction identified an incommensurate (δ_2, δ_2,0) magnetic structure below $T_{N1} = 15.4$ K with a change to (δ_1,0,0) at $T_{N3} = 12.2$ K, but saw no distinct changes at either $T_{N2} = 13.2$ K or $T_{N4} = 10.0$ K [11]. Our recent ^{151}Eu Mössbauer study confirmed that the initial ordering at T_{N1} is to a sinusoidally modulated incommensurate structure and that the modulation becomes fully square-wave below T_{N3} (unfortunately, ^{151}Eu Mössbauer spectroscopy cannot distinguish incommensurate and commensurate square-wave structures) [12].

Given the significant differences between the isostructural $EuAl_4$ and $EuGa_4$ compounds and the apparent paucity of data on the $EuIn_4$ system, we felt that a more detailed investigation of $EuIn_4$ was in order. Here we present bulk studies (transport, magnetometry, and heat capacity) combined with ^{151}Eu Mössbauer spectroscopy. We find evidence for two closely spaced magnetic transitions (at ∼10 K and ∼11 K) and an additional, possibly structural transition at ∼130 K which may also be due to two closely spaced and clearly nonmagnetic events.

II. EXPERIMENTAL METHODS

The growth sequence used here was based on the one previously employed to prepare single crystals of $EuAl_4$ and $EuGa_4$ [12]. A starting composition of $EuIn_9$ (Eu ingot, 99.9% Thermo Fisher Scientific, US; In grains, 99.9999% Johnson Matthey, UK) was loaded into a fritted alumina Canfield crucible set (CCS) [13,14] and sealed into a fused silica tube with a partial pressure of helium for thermal exchange. Following an homogenising anneal at 1000°C for three hours, the mixture was cooled to 700°C over five hours and decanted by centrifuging [15]. This step removes any high melting point materials (typically, oxide contaminants) that could provide nucleation sites leading to small crystals. These solid impurities can also make it more difficult to collect clean crystals as they remain in the growth crucible along with the target material. The collected liquid fraction was reloaded into a sealed fused silica tube with a fresh frit and catch crucible. It was remelted by heating to 800°C where it was held for two hours, then cooled to 550°C over two hours, and finally slow-cooled to 300°C over 250 hours, followed by decanting to recover the crystals.

Faceted mm-sized flat crystals were obtained, and phase identity was confirmed by Cu-K_α powder X-ray diffraction. X-ray diffraction measurements were made on a Bruker Phaser-II diffractometer using a Cu-K_α source. The sample used was hand-ground in a nitrogen-filled glovebox and

*Contact author: dhryan@physics.mcgill.ca

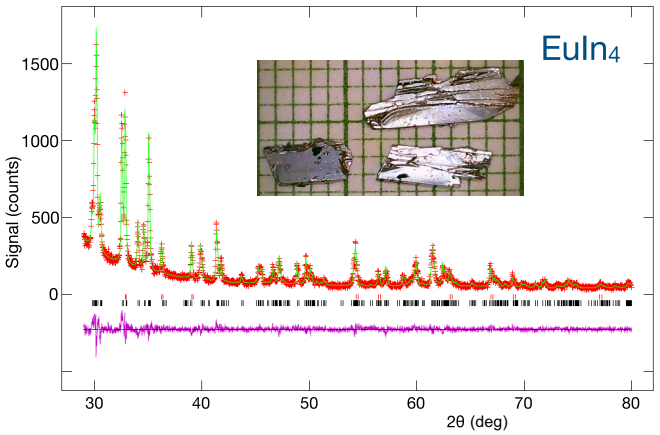

FIG. 1. X-ray diffraction pattern for $EuIn_4$ with the Rietveld refinement shown in green and the residuals shown below in purple. Bragg markers are for the ∼15 wt.% residual indium flux (red) and the primary $EuIn_4$ phase (black). The pattern has been truncated just below $2\theta = 30°$, as there was a significant background from the 8 μm Kapton cover. The inset shows some typical crystal flakes on mm graph paper.

covered with an 8 μm–thick Kapton sheet to limit oxidation during the measurement. Rietveld refinement of the diffraction patterns was carried out using the GSAS/EXPGUI packages [16,17]. The fitted lattice parameters given below are consistent with the previous report [6]. As indium has a strong tendency to wet the crystal surfaces, we were unable to completely remove all of the flux, and so the measured diffraction patterns always showed a significant (∼15 wt.%) indium contribution. This surface coating of indium also shorted out the transport measurements when it went superconducting below 3.4 K. [18].

Temperature- and magnetic field–dependent magnetization measurements ($1.8K \leqslant T \leqslant 300K$, $0T \leqslant \mu_0 H \leqslant 7T$) were performed using a Quantum Design MPMS-3 SQUID magnetometer. A half-cylindrical quartz sample holder was used for measurements with the field applied in the plane of the crystal. For those measurements made with applied field perpendicular to the plane of the sample, a small L-shaped adapter made out of 0.05 mm thick copper foil was used [19]. The measurements were performed in DC mode with the temperature stabilized at each point.

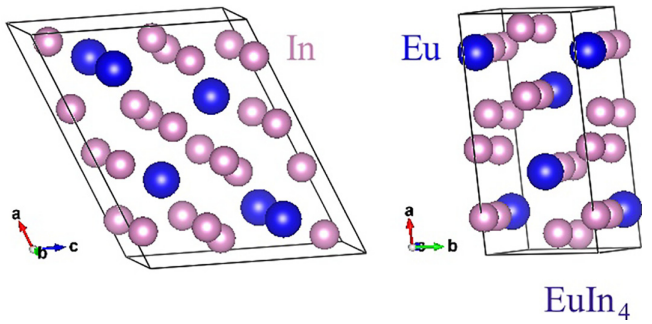

FIG. 2. Two projections of the monoclinic ($C2/m$ #12) unit cell of $EuIn_4$ based on the stucture published by Fornasini and Cirafici [6] and drawn using VESTA [23].

Low-temperature heat capacity measurements were made using semiadiabatic thermal relaxation technique as implemented in the heat capacity option of a Quantum Design Physical Property Measurement System (PPMS). A ∼8 mg sample with at least one flat surface was mounted on a microcalorimeter platform using Apiezon N grease. The addenda (platform + grease) heat capacity was measured separately for each sample and subtracted from the total heat capacity using the PPMS software. The ACT option of the PPMS instrument was used to perform the AC electrical transport measurements at a cooling rate of 0.5 K/min. Contacts to the sample were attached in a standard close to linear arrangement with Epotek H20E silver epoxy. The contact resistance was $\leqslant 1\ \Omega$.

^{151}Eu Mössbauer spectroscopy measurements were carried out on a conventional spectrometer driven in sinusoidal mode and calibrated using a standard ^{57}CoRh /α-Fe foil. Isomer shifts are quoted relative to EuF_3 at ambient temperature. ∼160 mg of $EuIn_4$ was hand-ground in an agate mortar under hexane to protect from oxidation. The powder was mixed with boron nitride to make a uniform absorber and loaded into a thin-window delrin holder. The sample was cooled in a vibration-isolated closed-cycle helium refrigerator. The simpler spectra were fitted to a sum of Lorentzian lines with the positions and intensities derived from a full solution to the nuclear Hamiltonian [20]. In cases where an incommensurate modulated magnetic structure was observed, the spectra were fitted using a distribution of hyperfine fields (B_{hf}) derived from an (assumed) sinusoidal modulation of the moments [21,22]. Departure from a purely sinusoidal modulation was allowed for by including higher harmonics (Bk_3, etc.) of the

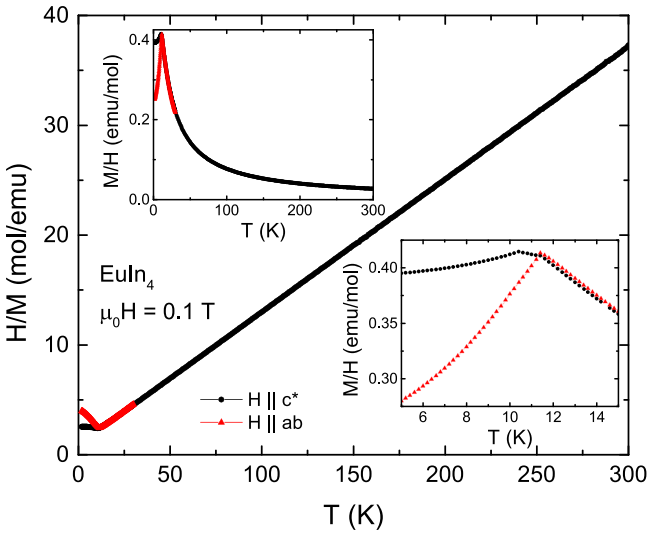

FIG. 3. Inverse DC susceptibility for $EuIn_4$ measured with a field of 0.1 T applied parallel to the c* direction (i.e. normal to the flake surface–black circles) and within the ab-plane (i.e. parallel to the flake surface–red triangles) showing clear Curie-Weiss behavior above the magnetic transition. All measurements were performed on cooling. The upper left inset presents the same data as M/H vs T showing a well-defined cusp marking the AF transition, while in the lower right inset, the region from 5 K to 15 K shows that the cusp is split when measured with the field along c*, but only the upper feature is apparent when the field is applied in the ab-plane.

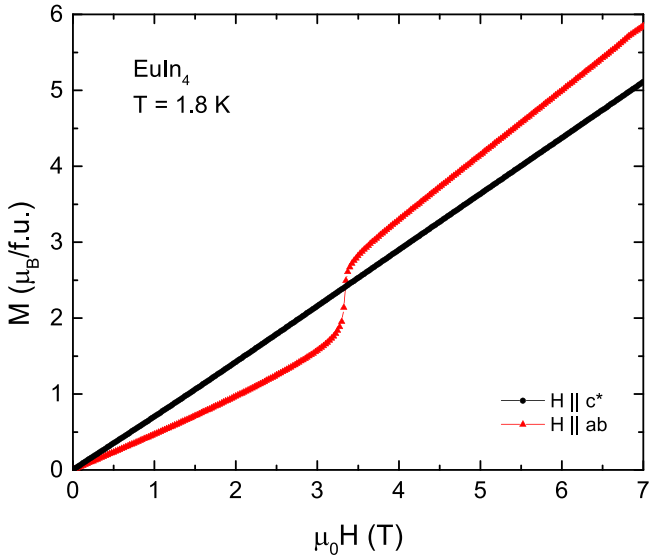

FIG. 4. Magnetisation curves at 1.8 K for $EuIn_4$ with the field applied parallel to the c* direction (black circles) and within the ab-plane (red triangles). The measurements were performed after cooling in zero field from T=30 K, i.e. above the magnetic transitions. A substantial fraction of the expected 7 μ_B/f.u. saturation moment is achieved in both directions. Whereas the behavior is essentially linear along the c* axis, there is a clear break near 3.5 T when the field is applied within the ab-plane.

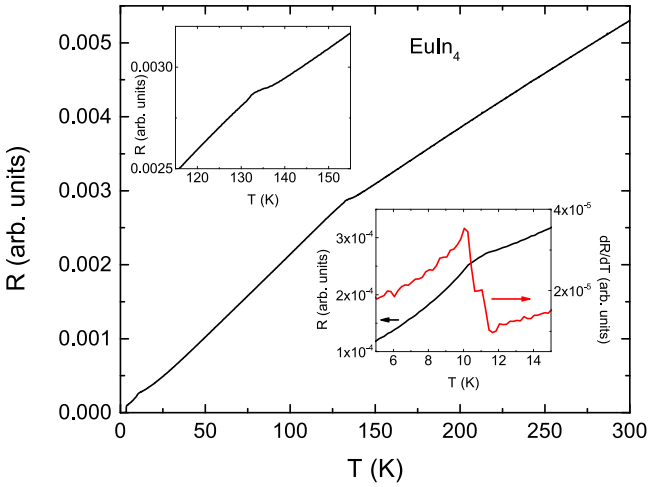

FIG. 5. Electrical transport measurements for $EuIn_4$ measured with the current along the long axis of a crystal flake. The abrupt drop in resistance near 3 K is the result of superconducting transition in the residual indium metal shorting out the $EuIn_4$ crystal. An expanded view of the region below 15 K is shown in the lower right inset where the split transition just above 10 K is apparent, particularly in the derivative shown in red. The inset to the upper left shows the feature near 135 K. Note: "arb. units" are used for the resistance, as there is an unknown contribution from residual indium that precludes an absolute determination of the sample resistance.

fundamental Bk_1. A constant term (Bk_0) was included to model the fully square-wave final state.

Low-temperature X-ray diffraction measurements were carried out at the Brockhouse Diffraction Sector of the Canadian Light Source (CLS) Saskatchewan, Canada. A crystal was hand-ground in a nitrogen-filled glovebox and loaded into a 0.5 mm i.d. Kapton tube and sealed with super glue. Measurements were made at a wavelength of 0.81966 Å with cooling provided by an Oxford Cryostream 800 Plus.

III. RESULTS

A. Bulk measurements

$EuIn_4$ grew as thin (< 1 mm) elongated plates that were several mm long (see inset to Fig. 1). The crystals were stable in air for a few days (likely because of a protective coating of excess indium) but were destroyed in minutes once powdered, exposing free surfaces to the air. Rietveld refinement of the X-ray diffraction pattern shown in Fig. 1 confirmed phase identity with indium metal being the only observed impurity. Fitted lattice parameters of $a = 11.948(1)$ Å, $b = 5.1078(2)$ Å and $c = 9.8826(5)$ Å with $\beta = 114.57(1)^\circ$ were consistent with the previous report [6]. Measurements on a single flake showed only $00l$ reflections indicating that the c* direction was perpendicular to the plates. Projections of the unit cell along the b and c axes are shown in Fig. 2.

Susceptibility measured in a DC-applied field of 0.1 T shows conventional Curie-Weiss behavior at high temperatures with an effective moment of 8.1 μ_B/Eu (slightly above the theoretical value of 7.94 μ_B/Eu) and a Weiss temperature of −7.4 K indicating divalent europium and dominant antiferromagnetic (AF) exchange (Fig. 3). However, as the lower right inset to Fig. 3 shows, a simple AF cusp is observed when the field is applied within the ab-plane, but when the field is applied parallel to the c* direction the peak is clearly split, showing two features ∼1 K apart. This provides the first indication that ordering in this system is more complex than the simple AF order seen in $EuGa_4$ [8].

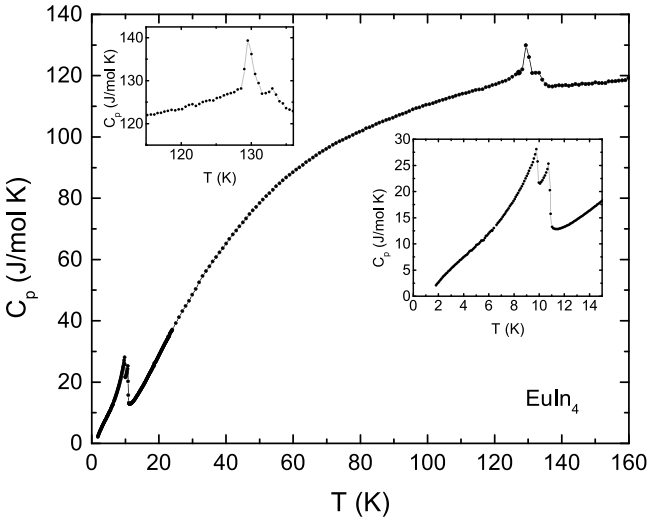

FIG. 6. Heat capacity for $EuIn_4$ showing the magnetic transitions near 10 K and the two events near 130 K. The two insets show expanded views of the region below 15 K (lower right) and the region around the 130 K events (upper left, taken from a second measurement run over a narrower temperature range). In both cases the split structure is clearly evident.

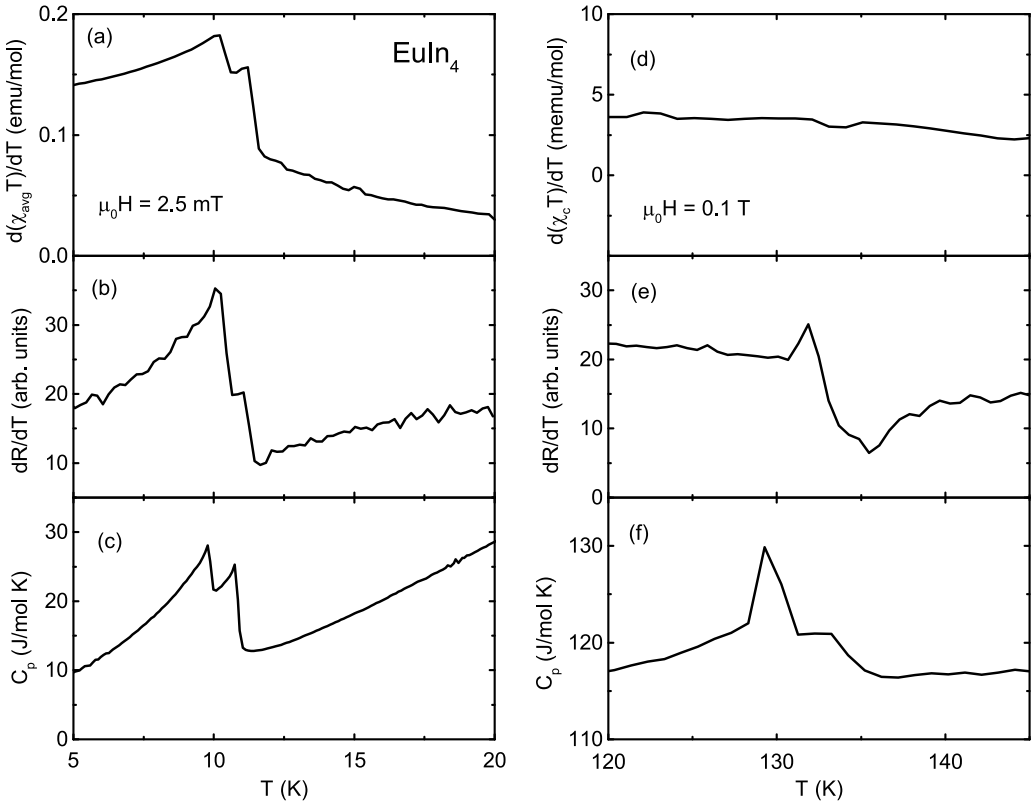

FIG. 7. Details of the two transition regions. Panels (a)–(c) show d(χ_{avg}T)/dT [24], dR/dT, and C_p(T) for the lower transition, and panels (d)–(f) show the same for the upper transition. Both transitions are clearly split, but there is no magnetic signature for the upper transition.

The magnetization at 1.8 K with the field applied parallel to the c* direction is essentially linear in field up to 7 Tesla, where it reaches about 70% of the expected 7 μ_B/f.u. saturation for Eu^{2+} (Fig. 4). With the field in the ab-plane, the slope is visibly lower, suggesting that c* is the easier direction (at least below 3 T). Above 3 T there is a clear step in M(T) above which the slope is clearly steeper. The field and temperature dependences of this and other features in the magnetisation curves are summarized in the Appendix (Fig. 19).

Electrical transport shown in Fig. 5 confirms the split transition near 10 K but also provides evidence for an additional feature near 135 K that was not apparent in the susceptibility data. Finally, heat capacity measurements clearly show that *both* the magnetic transition near 10 K and the feature at 135 K are split (Fig. 6).

Gathering all of the bulk data on the two transition regions in Fig. 7 shows the consistency between the measurements. All three data sets for the lower transition show that it is clearly split, and although the peaks in C_p(T) occur at slightly lower (∼0.3 K) temperatures than those seen in d(χ_{avg}T)/dT [24] and dR/dT, the gap between the two features is still ∼1 K. Since the features in d(χ_{avg}T)/dT and dR/dT are in better agreement, we take them as the locations of the two magnetic transitions, yielding $T_{N1} = 11.1$ K and $T_{N2} = 10.1$ K. By contrast, the corresponding measurements around the upper transition [Figs. 7(d)–7(f)] show somewhat poorer correspondence between the transition temperatures inferred from dR/dT and C_p(T), but more significantly, there is no discernible feature in the magnetic susceptibility at either event. Using the peaks in C_p(T), we estimate that the two upper events occur at $T_{E1} = 133$ K and $T_{E2} = 129$ K. The absence of any susceptibility feature around T_{E1} or T_{E2} [Fig. 7(d)] suggests that the events at ∼130 K are not magnetic in origin. Furthermore, the relatively sharp form of the double-peaked feature in the heat capacity combined with the shape of the corresponding anomaly in resistance suggest that they are the signatures of structural phase transition(s), rather than reflecting the formation of a charge density wave (CDW). The change in the Hall resistivity at about 135 K (see Fig. 16) is consistent with a possible structural transition and the resulting change in the band structure.

B. ^{151}Eu Mössbauer spectroscopy

For further insights into the magnetic ordering in $EuIn_4$, we turn to ^{151}Eu Mössbauer spectroscopy. The spectrum at 15 K, well above the magnetic transitions, shows a simple paramagnetic spectrum with an isomer shift of −11.42(1) mm/s, confirming that the europium is definitely divalent [25] (Fig. 8). A small quadrupole contribution (conventionally defined as e^2qQ, where e is the electron charge, Q is the quadrupole moment of the ^{151}Eu nucleus in its ground state, and eq is maximum value of the electric field gradient at the nucleus) of −3.7(5) mm/s is also apparent. The feature just right of 0 mm/s is a trivalent contamination most likely introduced during mounting. As noted above, the powdered material is extremely air-sensitive, and varying amounts of this trivalent component were encountered. Here it accounts for 9.0(6)% of the total signal. The trivalent impurity does not significantly impact the analysis, as it is nonmagnetic

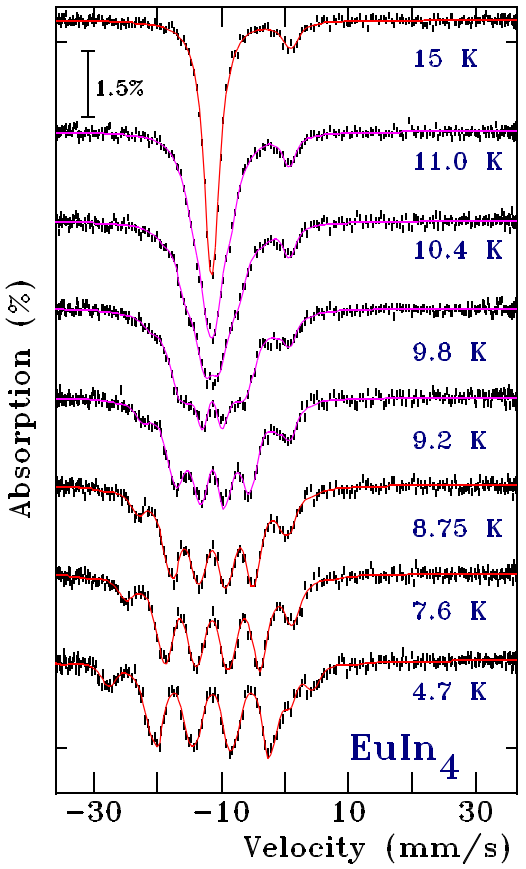

FIG. 8. ^{151}Eu Mössbauer spectra of $EuIn_4$ showing the evolution of the spectra with temperature. The lines clearly broaden on warming, and the spectra develop a characteristic "droop" towards the center. The solid red lines through the lower and highest temperature spectra are fits derived from the full Hamiltonian solution, whereas the magenta lines through the remaining, intermediate temperature spectra are fits derived from the incommensurate modulation model (see text for details of both models).

at all temperatures, so its position and width are essentially temperature-independent. The trivalent impurity was included in all of the fits shown here. Cooling to 4.7 K leads to a clear magnetic splitting with a hyperfine field of 22.17(7) T, significantly lower than that seen in $EuAl_4$ [26.55(4) T] or $EuGa_4$ [26.56(6) T] [12]. The temperature evolution of the spectra on warming is initially quite normal, and the spectra can be fitted using the expected full Hamiltonian solution [20] with the quadrupole contribution fixed at the value found at 15 K. However, above about 9 K, the quality of the fits becomes noticeably poorer, and there is a rapid increase in the fitted linewidth (Fig. 9). Fitting the break in the linewidth vs temperature gives a transition temperature of 9.4(1) K, close to T_{N2} derived above from bulk measurements, suggesting that there is a significant change in the nature of the magnetic order at T_{N2}.

The evolution of the spectra on warming through 9 K suggests the development of an incommensurate modulated ordering of the europium moments. The lines clearly broaden and the spectra develop a characteristic "droop" towards the center, as the central doublet appears to extend below the

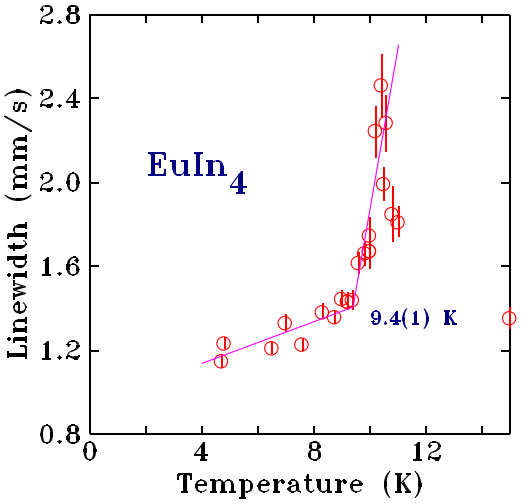

FIG. 9. Evolution of the fitted linewidth (half-width half-maximum) using a single-site full Hamiltonian model to fit the spectra. Note the clear break near 9.4 K where the fitted linewidth starts to increase rapidly. The point at 15 K in the paramagnetic state confirms that the linewidth recovers once the magnetic contributions are absent.

lines to their immediate left and right (all four are normally approximately the same intensity). To fit these spectra, we assume that the moment modulation along the direction of the propagation vector **k** can be written in terms of its Fourier components, and we further assume that the observed hyperfine field is a linear function of the magnitude of the Eu moment at any given site. The variation of B_{hf} with distance

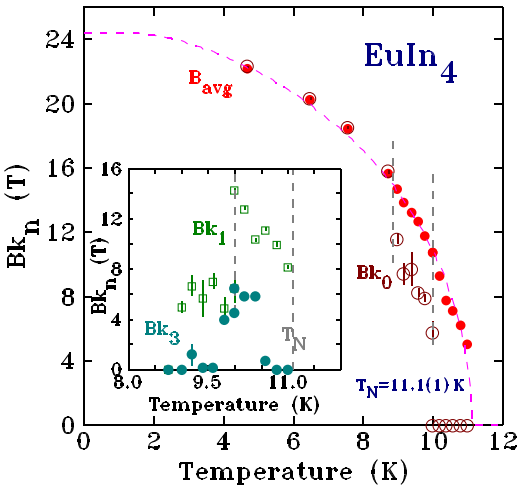

FIG. 10. Temperature dependence of the average hyperfine field (B_{avg}) and three Fourier components (Bk_0, Bk_1, and Bk_3) for $EuIn_4$ derived from the incommensurate modulated model described in the text. Fitting a $J = \frac{7}{2}$ mean-field model through $B_{avg}(T)$ yields a transition temperature of 11.1(1) K, consistent with T_{N1} derived from bulk data. The two vertical dashed lines mark the onset of the constant term (Bk_0) at 10 K (corresponding with T_{N2}) and the end of the modulated order at 8.8 K. The inset shows the behavior of the fundamental (Bk_1) and harmonic (Bk_3) terms, with vertical dashed lines marking T_{N1} at 11.1(1) K and T_{N2} at 10.1 K.

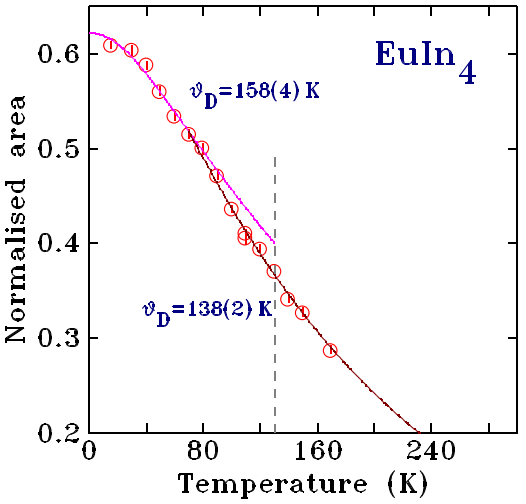

FIG. 11. Temperature dependence of the normalized spectral area (proportional to the $f-$factor) for $EuIn_4$. The vertical dashed line at 130 K marks the approximate position of the high-temperature event seen in the transport (Fig. 5) and heat capacity (Fig. 6) measurements. A hardening of the lattice is apparent on cooling through 80 K as the Debye temperature (ϑ_D) is more than 10% higher below about 80 K.

x along the propagation vector $\mathbf{k}$ can then be written as [22]

$$B_{hf}(kx) = Bk_0 + \sum_{l=0}^{\infty} Bk_{2l+1} \sin[(2l+1)kx], \qquad (1)$$

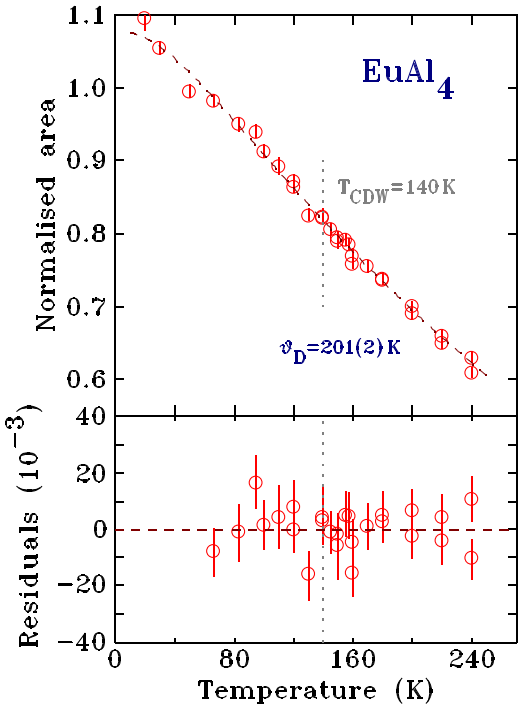

FIG. 12. Normalised spectral area for $EuAl_4$ showing a fit to conventional Debye behavior. Residuals are shown in the lower panel. There is no apparent deviation at T_{CDW} (shown as a vertical dashed line), suggesting that the CDW transition does not involve a significant change in the phonon spectrum at the Eu site.

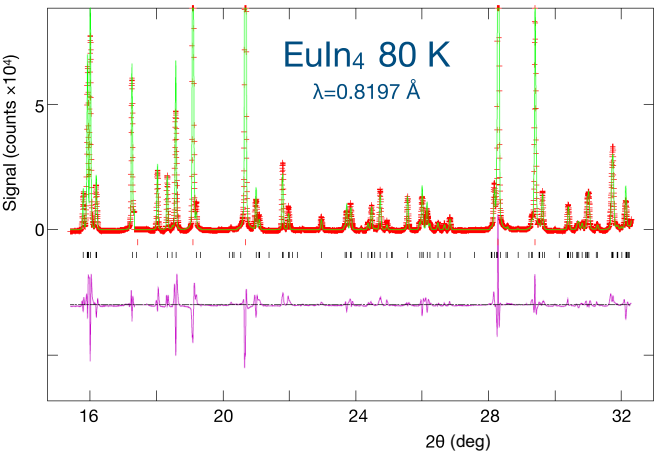

FIG. 13. X-ray diffraction pattern at 80 K for $EuIn_4$ measured at a wavelength of 0.8197 Å. The fit includes only monoclinic $EuIn_4$ (lower Bragg markers) and elemental indium (upper Bragg markers).

where the Bk_{2l+1} are the odd Fourier coefficients of the field (moment) modulation. As $+B_{hf}$ and $-B_{hf}$ are indistinguishable, kx needs to run over only half the modulation period, and in this case, a square-wave modulated structure can be modeled either as a sum over a very large number of Fourier coefficients, or by simply using the Bk_0 term with all of the other Bk_n set to zero. We have found that fits are far more stable with the Bk_0 term included, rather than using a large set of Bk_n; however, the two approaches are effectively equivalent. Variations of this model have also been used to fit spectra of EuPdSb [22], Eu_4PdMg [26], and $EuAl_4$ [12]. The effects of the small quadrupole contribution were not included in the modulated model, as (a) the effects even in the 5 K spectrum were minor; and (b) the spectral broadening washes out most of the details.

The results of these modulated fits are shown as magenta lines in Fig. 8, while the full Hamiltonian fits at the high (paramagnetic) and low temperatures are shown as red lines.

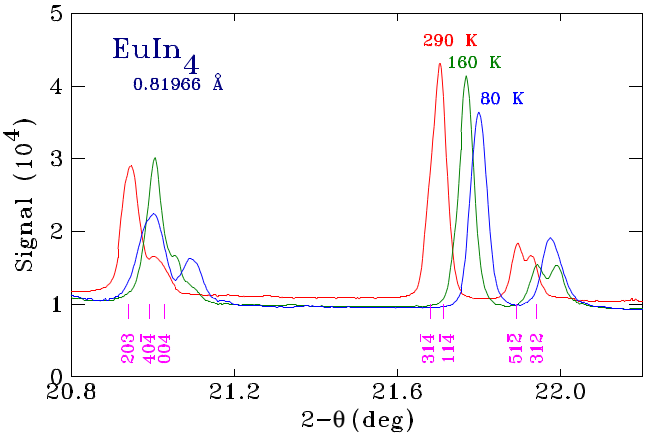

FIG. 14. Selected region of the low-temperature X-ray diffraction patterns showing the evolution of the peak positions on cooling but no significant changes beyond a slight broadening of the peaks at the lowest temperature. Bragg markers and labels are shown for the 290 K pattern only.

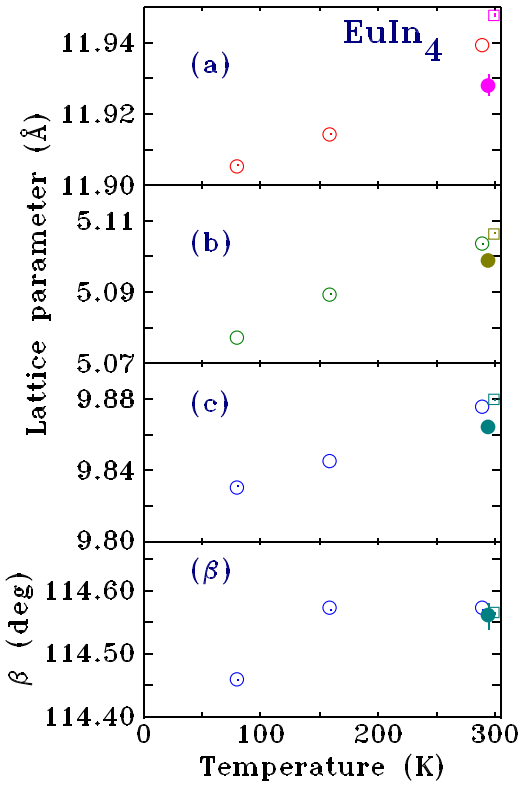

FIG. 15. Lattice parameters (a, b, and c, and the monoclinic angle β) derived from fits to low-temperature X-ray diffraction patterns. Open circles show a, b, c, and β for the monoclinic ($C2/m$ #12) $EuIn_4$ at 290 K, 160 K, and 80 K. Solid circles show values from Fornasini and Cirafici [6], while the open squares show our values derived from the data taken on the Bruker instrument. In most cases, the uncertainties are smaller than the symbols and many are too small to appear.

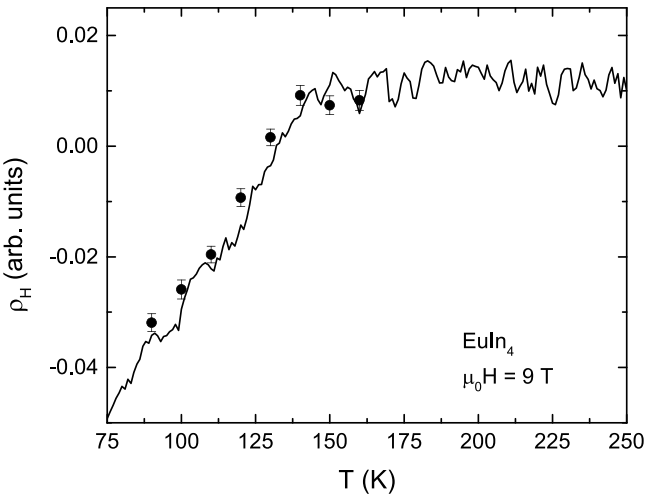

FIG. 16. Temperature dependence of the Hall resistance (ρ_H) for $EuIn_4$ showing the effects of the structural transition at ~135 K. The solid line was obtained from temperature sweeps in a field of 9 T, while the points show the results from field sweeps at fixed temperature.

Plotting the various components derived from the fits vs temperature in Fig. 10 provides some insights into the nature of the magnetic order in $EuIn_4$. Fitting the temperature dependence of the average hyperfine field (B_{avg}) to a $J = \frac{7}{2}$ mean-field model appropriate for Eu^{2+} yields a transition temperature of 11.1(1) K consistent with T_{N1} derived from bulk data above. The initial modulation of the order appears to be purely sinusoidal, as only the fundamental Bk_1 term is nonzero (inset to Fig. 10). On further cooling, the first harmonic, Bk_3, develops, and finally, below 10 K we must include the constant term, Bk_0. The temperature at which the Bk_0 term becomes necessary appears to correspond to T_{N2}, but there is one final change to the order that does not appear to have a C_p(T), R(T), or χ(T) signature: By 8.8 K all signs of the modulated order are lost, and a simple, single-site model with no hyperfine field distribution fits the spectra with reasonable linewidths. We emphasize that incommensurate modulated ordering in europium intermetallic compounds, while common, is not always present, and $EuGa_4$ provides a recent example of "simple" behavior [12]. Finally, that a single-site model fits the lowest temperature spectra does not necessarily mean that the magnetic order is now *commensurate*. Any magnetic structure in which the europium ions all have the same moment *magnitude* will yield a simple, sharp spectrum, especially if the moment *directions* all make the same angle with respect to the principal axis of the local electric field gradient. This situation is clearly illustrated by $EuIn_2$, which follows a similar modulated (below 14 K) to squared-up (below 9 K) ordering path as the current $EuIn_4$, but X-ray resonant magnetic scattering (XRMS) shows that the order remains incommensurate down to at least 5 K [27].

As shown above, both R(T) (Fig. 5) and C_p(T) (Fig. 6) show evidence for an additional feature at about 130 K. As there is no magnetic contribution to the ^{151}Eu Mössbauer spectra above T_{N1} (Fig. 8), and susceptibility does not exhibit any apparent deviations from simple Curie-Weiss behavior up to 300 K [Fig. 7(d)], we can rule out magnetic effects as the origin of the 130 K feature. At fixed experimental geometry, the integrated area of a Mössbauer spectrum divided by the baseline of the spectrum is proportional to the recoil-free fraction or $f-$factor. The $f-$factor decreases with increasing temperature as the thermally driven amplitude of the atomic vibrations increases. If we assume a simple Debye model for the vibration amplitudes, then the temperature dependence of the normalized spectral area can be fitted to derive an effective Debye temperature (ϑ_D). Data for $EuIn_4$ are shown in Fig. 11. We found that a single Debye temperature does not fit the measured data, and the observed area progressively falls away from the low-temperature extrapolation. The deviation is well outside uncertainty by 100 K, but likely starts below that. Figure 11 shows a simple two–ϑ_D fit to the data indicating there is a clear hardening of the lattice in the 80 K–100 K temperature range. This range is somewhat below the 130 K derived from R(T) and C_p(T), and this may reflect the differing sensitivities of the techniques.

For comparison, $EuAl_4$ is known to exhibit a charge density wave (CDW) transition at ~140 K [7,10]. Examination of the temperature dependence of the normalized spectral area for $EuAl_4$ shows no deviation at T_{CDW}, and the evolution

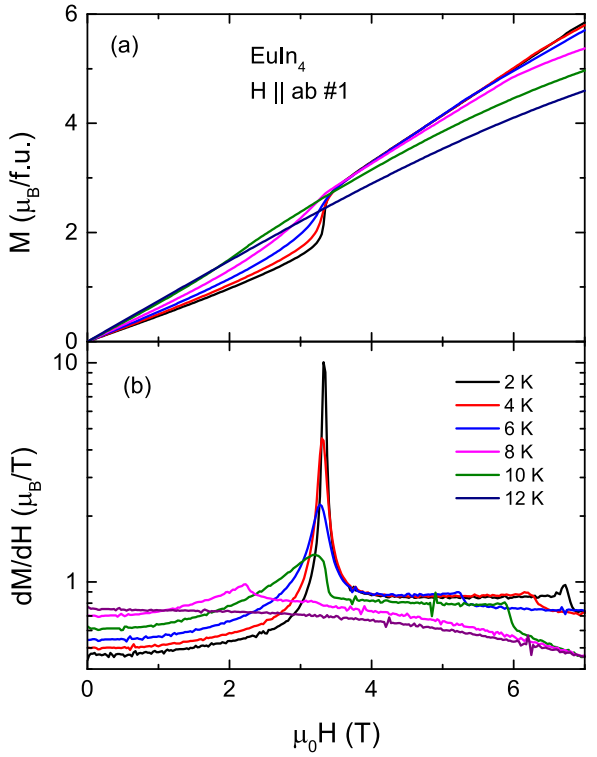

FIG. 17. Some typical data used to locate transitions in the M–H–T behavior of $EuIn_4$: (a) M vs H for $EuIn_4$ with the field applied within the sample plane, parallel to the crystallographic ab-plane and thus perpendicular to the c* axis). (b) the first derivative of the data presented in (a). Note: similar data were obtained with the field applied in a second (perpendicular) direction within the ab-plane, and with the field applied parallel to the c* axis.

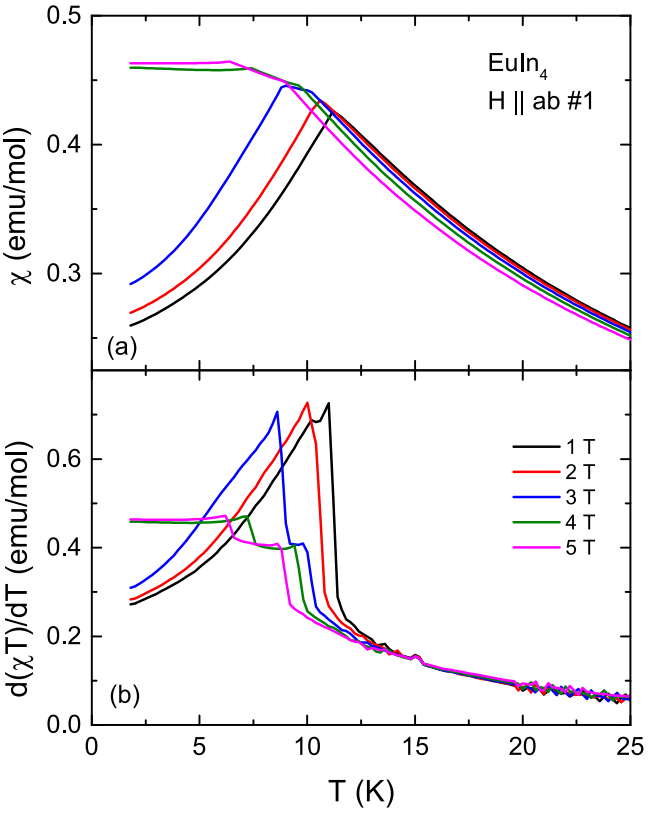

FIG. 18. Some typical data used to locate transitions in the M–H–T behavior of $EuIn_4$: (a) χ vs T for $EuIn_4$ with the field applied within the sample plane, parallel to the crystallographic ab-plane and thus perpendicular to the c* axis). (b) $d(\chi T)/dT$ for the data presented in (a). Note: similar data were obtained with the field applied in a second (perpendicular) direction within the ab-plane, and with the field applied parallel to the c* axis.

of the area can be fitted over the whole range from above $T_{N1} = 15.4$ K to 240 K using a *single* value of 201(2) K for ϑ_D (Fig. 12). The clear contrast between $EuAl_4$, where a confirmed CDW transition does not affect the Mössbauer-derived ϑ_D, and the current case of $EuIn_4$, where we see a clear departure from a simple Debye dependence, reinforces our earlier position that the 130 K event in $EuIn_4$ is not due to a CDW transition.

C. Low-temperature powder x-ray diffraction measurements

A preliminary search for evidence of a structural transition associated with the 130 K events was unsuccessful. The only reflections observed could be assigned either to the monoclinic structure ($C2/m$ #12) [6] of $EuIn_4$ observed at ambient temperatures or to residual indium flux. Figure 13 shows the fitted diffraction pattern taken at 80 K. No new peaks were observed on cooling, and the diffraction pattern could be fitted as a combination of monoclinic $EuIn_4$ and residual indium flux. Figure 14 presents a narrow section of the diffraction patterns (chosen to have several distinct peaks with limited overlap and no contribution from the residual indium flux) at the three temperatures measured showing the expected shift to higher diffraction angles as the cell contracts on cooling. No significant changes in the patterns were observed, beyond a slight broadening at the lowest temperature (80 K). The lattice parameters derived from the Rietveld analysis are shown in Fig. 15, and other than the expected slow contraction on cooling, there do not appear to be any significant changes. The diffraction patterns at all three temperatures could be fitted as a combination of monoclinic $EuIn_4$ and elemental indium. The greater precision provided by single-crystal diffraction measurements will likely be needed to establish the nature of the 130 K events.

IV. CONCLUSIONS

$EuIn_4$ initially adopts an incommensurate sinusoidally modulated magnetic structure below $T_{N1} = 10.8$ K, and this order rapidly squares up on cooling through $T_{N2} = 9.8$ K, although it may remain incommensurate. Two other transitions that have no magnetic signatures were identified in transport and heat capacity data near 130 K. A preliminary search for structural changes through the 130 K events was unsuccessful. Neutron diffraction or XRMS measurements would be needed to determine the detailed magnetic structure adopted by the europium moments in $EuIn_4$, while single-crystal X-ray diffraction measurements would be needed to understand the changes that occur at the 130 K events.

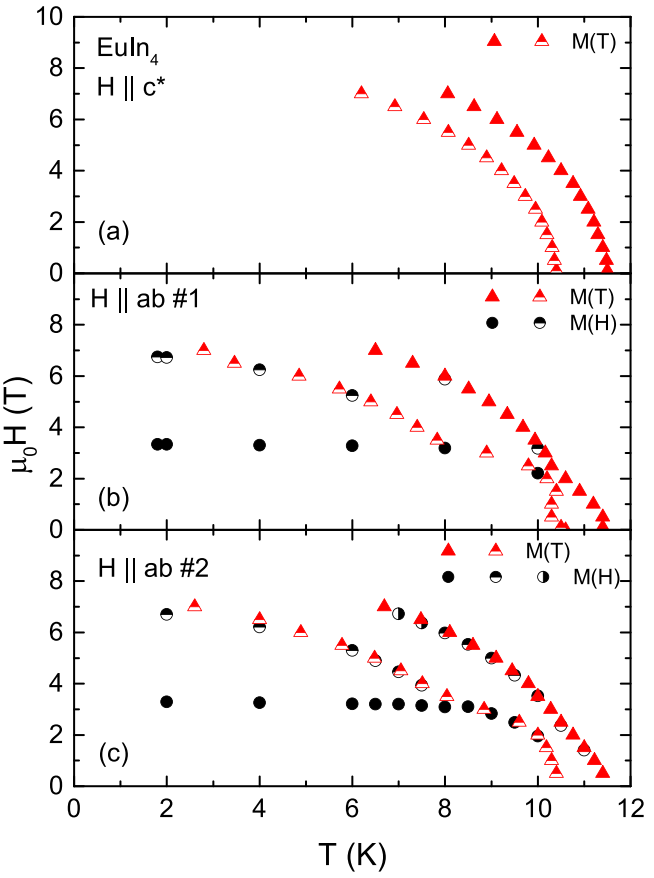

FIG. 19. Anisotropic magnetic transition diagrams obtained with the field applied along (a) the c* axis; (b), and (c) along two mutually orthogonal directions perpendicular to the c* axis. Examples of the data used to construct these figures are shown in Figs. 17 and 18.

ACKNOWLEDGMENTS

Financial support for this work was provided by Fonds Québécois de la Recherche sur la Nature et les Technologies, and the Natural Sciences and Engineering Research Council (NSERC) Canada. Work at Ames National Laboratory is supported by the Office of Basic Energy Sciences of the U.S. Department of Energy, Division of Materials Sciences and Engineering under Contract No. DE-AC02-07CH11358 with Iowa State University.

Part of the research described in this paper was performed at the Canadian Light Source, a national research facility of the University of Saskatchewan, which is supported by the Canada Foundation for Innovation (CFI), the NSERC, the National Research Council (NRC), the Canadian Institutes of Health Research (CIHR), the Government of Saskatchewan, and the University of Saskatchewan. The assistance provided by Adam Leontowich is gratefully acknowledged.

APPENDIX A: HALL RESISTIVITY THROUGH THE POSSIBLE STRUCTURAL TRANSITION

Hall resistance (ρ_H) of $EuIn_4$ was measured near the suspected structural transition(s). Temperature sweeps were made with both positive and negative magnetic fields applied along the c* axis, and the two runs were combined to recover ρ_H and exclude any possible magnetoresistance contribution due to the inevitable misalignment of the voltage contacts. These results are shown as a solid line in Fig. 16. As a cross-check, several data points were also taken using a field sweep at fixed temperature, where the Hall resistance was extracted as the slope of the field-dependent voltage. These are shown as points on Fig. 16. It is apparent that the effects of the structural transition are seen in the ρ_H(T) data, as well as in C_p(T) and R(T).

APPENDIX B: ANISOTROPIC H–T TRANSITION DIAGRAMS

Measuring magnetization as a function of field at fixed temperature (Fig. 17) or the susceptibility as a function of temperature at fixed field (Fig. 18) reveals several features [clearer in the derivative plots Fig. 17(b) and Fig. 18(b)]. The results of these measurements are gathered in Fig. 19 as anisotropic H–T transition diagrams (H ∥ c*, and two mutually orthogonal directions each perpendicular to the c* axis). Whereas for H ∥ c* the two magnetic transitions decrease with field in almost parallel fashion, more complex (with three to four different phases), somewhat anisotropic transition diagrams are constructed for H ∥ a-b. Further neutron scattering would be required to understand the nature of these phases.

[1] C. C. Chao and P. Duwez, J. Appl. Phys. **37**, 2631 (1966).
[2] A. Iandelli and A. Palenzona, J. Less-Common Met. **9**, 1 (1965).
[3] A. Iandelli, Z. Anorg. Allg. Chem. **330**, 221 (1964).
[4] J. L. Moriarty, J. E. Humphreys, R. O. Gordon, and N. C. Baenzinger, Acta Cryst. **21**, 840 (1966).
[5] A. Palenzona, J. Less-Common Met. **10**, 290 (1966).
[6] M. L. Fornasini and S. Cirafici, Z. Kristallogr. - Cryst. Mater. **190**, 295 (1990).
[7] S. Shimomura, H. Murao, S. Tsutsui, H. Nakao, A. Nakamura, M. Hedo, T. Nakama, and Y. Ōnuki, J. Phys. Soc. Jpn. **88**, 014602 (2019).
[8] A. Nakamura, Y. Hiranaka, M. Hedo, T. Nakama, Y. Miura, H. Tsutsumi, A. Mori, K. Ishida, K. Mitamura, Y. Hirose, K. Sugiyama, F. Honda, R. Settai, T. Takeuchi, M. Hagiwara, T. D. Matsuda, E. Yamamoto, Y. Haga, K. Matsubayashi, Y. Uwatoko *et al.*, J. Phys. Soc. Jpn. **82**, 104703 (2013).
[9] T. Kawasaki, K. Kaneko, A. Nakamura, N. Aso, M. Hedo, T. Nakama, T. Ohhara, R. Kiyanagi, K. Oikawa, I. Tamura, A. Nakao, K. Munakata, T. Hanashima, and Y. Ōnuki, J. Phys. Soc. Jpn. **85**, 114711 (2016).
[10] A. Nakamura, T. Uejo, F. Honda, T. Takeuchi, H. Harima, E. Yamamoto, Y. Haga, K. Matsubayashi, Y. Uwatoko, M. Hedo, T. Nakama, and Y. Ōnuki, J. Phys. Soc. Jpn. **84**, 124711 (2015).
[11] K. Kaneko, T. Kawasaki, A. Nakamura, K. Munakata, A. Nakao, T. Hanashima, R. Kiyanagi, T. Ohhara, M. Hedo, T. Nakama, and Y. Ōnuki, J. Phys. Soc. Jpn. **90**, 064704 (2021).

[12] D. H. Ryan, B. Kuthanazhi, N. H. Jo, and P. C. Canfield, AIP Adv. **14**, 015239 (2024).
[13] P. C. Canfield, T. Kong, U. S. Kaluarachchi, and N. H. Jo, Philos. Mag. **96**, 84 (2016).
[14] LSP Industrial Ceramics, Inc., Canfield crucible sets (2024), https://www.lspceramics.com/canfield-crucible-sets-2/.
[15] P. C. Canfield, Rep. Prog. Phys. **83**, 016501 (2020).
[16] A. C. Larson and R. B. Von Dreele, Los Alamos National Laboratory Report LAUR 86-748 (2000).
[17] B. H. Toby, J. Appl. Crystallogr. **34**, 210 (2001).
[18] This is consistent with essentially zero solubility for europium in indium.
[19] S. L. Bud'ko, M. Xu, and P. C. Canfield, Supercond. Sci. Technol. **36**, 115001 (2023).
[20] C. J. Voyer and D. H. Ryan, Hyperfine Interact. **170**, 91 (2006).
[21] A. Maurya, P. Bonville, A. Thamizhavel, and S. K. Dhar, J. Phys.: Condens. Matter **26**, 216001 (2014).
[22] P. Bonville, J. A. Hodges, M. Shirakawa, M. Kasaya, and D. Schmitt, Eur. Phys. J. B **21**, 349 (2001).
[23] K. Momma and F. Izumi, J. Appl. Crystallogr. **44**, 1272 (2011).
[24] The approximate polycrystalline average susceptibility, χ_{avg}, was calculated as $(\chi_{c*} + 2\ \chi_{ab})/3$.
[25] F. Grandjean and G. J. Long, Mössbauer spectroscopy of europium-containing compounds, in *Mössbauer Spectroscopy Applied to Inorganic Chemistry*, edited by G. J. Long and F. Grandjean, Modern Inorganic Chemistry, Vol. 3 (Plenum Press, NY, 1989), Chap. 11, pp. 513–597.
[26] D. H. Ryan, A. Legros, O. Niehaus, R. Pöttgen, J. M. Cadogan, and R. Flacau, J. Appl. Phys. **117**, 17D108 (2015).
[27] B. Kuthanazhi, S. X. M. Riberolles, D. H. Ryan, P. J. Ryan, J.-W. Kim, L.-L. Wang, R. J. McQueeney, B. G. Ueland, and P. C. Canfield, Phys. Rev. B **109**, 214401 (2024).